



Cite this: *RSC Adv.*, 2025, 15, 38036

# A high-performance solar blind photodetector based on spinel gallium oxide thin film supported by aluminum doping

Yuehua An,<sup>a</sup> Wei Cui,<sup>a</sup> Jiangwei Liu,<sup>a</sup> Pengcheng Xu,<sup>a</sup> Zhensen Gao <sup>\*bc</sup> and Weihua Tang<sup>\*d</sup>

Metastable  $\gamma$ -phase gallium oxide ( $\text{Ga}_2\text{O}_3$ )-based semiconductor materials have recently garnered much attention for developing high-performance wide-band-gap optoelectronic devices. However, the difficulty in the synthesis of single-phase crystals and the poor thermal stability of metastable  $\gamma$ - $\text{Ga}_2\text{O}_3$  pose great obstacles for its potential applications. In this work, we experimentally demonstrate the epitaxial growth of  $\gamma$ - $\text{Ga}_2\text{O}_3$  thin films at 750 °C on  $\alpha$ - $\text{Al}_2\text{O}_3$  (0001) substrates upon aluminum (Al) doping. A solar blind photodetector based on an Al-doped  $\gamma$ - $\text{Ga}_2\text{O}_3$  thin film was successfully fabricated, and its properties were investigated in detail. Benefiting from its high crystal quality and absence of oxygen vacancies in Al-doped  $\gamma$ - $\text{Ga}_2\text{O}_3$ , the solar blind photodetector exhibited a very low dark current, fast decay time, high detectivity, and excellent wavelength selectivity, along with high stability and reproducibility. Notably, the present device exhibited no obvious performance degradation when the light intensity and bias voltage were increased, indicating good self-heating dissipation, which is beneficial for future practical applications. The  $\gamma$ - $\text{Ga}_2\text{O}_3$  thin film-based photodetector might open up new possibilities to obtain high-performance thin film-based solar blind ultraviolet optoelectronic devices.

Received 29th August 2025  
Accepted 27th September 2025

DOI: 10.1039/d5ra06475a

rsc.li/rsc-advances

## 1. Introduction

Solar-blind ultraviolet (UV) detection with a cutoff wavelength shorter than 280 nm has a vast and growing number of military and civil surveillance applications, such as missile tracking, short-range secure communication, UV astronomy, ozone hole monitoring, and corona detection.<sup>1–5</sup> Commercial solar blind photodetectors (PDs) are mainly based on vacuum photo-multiplier tubes, which have obvious disadvantages, such as high operation power consumption, inflexibility, and difficulty in integration, thereby limiting their practical applications.<sup>6</sup>

Recently, solar blind PDs based on wide-bandgap semiconductors, such as AlGaIn, MgZnO, diamond, and  $\text{Ga}_2\text{O}_3$ , have attracted great attention.<sup>7–10</sup> However, high-quality epitaxial AlGaIn films are difficult to be prepared due to their crystal deterioration with increasing Al content and the breakdown of

the single wurtzite phase of MgZnO with increasing Mg content, and diamonds cannot be used to detect the entire solar-blind UV region because of their non-tunable bandgap.<sup>10,11</sup>  $\text{Ga}_2\text{O}_3$  with a direct bandgap of 4.9–5.3 eV lies sharply in the solar-blind spectrum region and also exhibits a flexible tunability in bandgap by alloying with different materials, making it one of the ideal candidates to fabricate solar-blind UV PDs.<sup>12–15</sup>  $\text{Ga}_2\text{O}_3$  is known to show five crystalline phases named  $\alpha$ ,  $\beta$ ,  $\gamma$ ,  $\delta$  and  $\epsilon$ .<sup>16</sup> Among these phases, the most stable monoclinic  $\beta$ - $\text{Ga}_2\text{O}_3$  has been widely studied. The solar-blind PDs based on  $\text{Ga}_2\text{O}_3$  are concentrated on  $\beta$ - $\text{Ga}_2\text{O}_3$  because of its stability and ease of preparation. However,  $\beta$ - $\text{Ga}_2\text{O}_3$  has a monoclinic structure, which makes it difficult to grow high-quality  $\beta$ - $\text{Ga}_2\text{O}_3$  on hetero-substrates. It is challenging to find material lattices matching with the  $\beta$ - $\text{Ga}_2\text{O}_3$  lattice to grow epitaxial thin films for optoelectronic applications. Thus, it is meaningful to explore the potential application of other metastable materials with a hexagonal/cubic structure, which have the same structure as those of  $\text{Al}_2\text{O}_3$ , ZnO, SiC, GaN and  $\text{MgAl}_2\text{O}_4$ .<sup>17–19</sup> PDs based on other metastable phases have rarely been reported because of the difficulty in synthesizing single-phase crystals with thermal stability.

A recent first-principles study on the energetics of the  $\text{Ga}_2\text{O}_3$  polymorphs suggests that the differences in free energy between the  $\beta$ -phase and other metastable phases are small; therefore, the polymorph of  $\text{Ga}_2\text{O}_3$  is selected depending upon the preparation conditions.<sup>20–22</sup> Moreover, doping is an important

<sup>a</sup>School of Optoelectronic Engineering, Guangdong Polytechnic Normal University, Guangzhou 510665, China

<sup>b</sup>Key Laboratory of Photonic Technology for Integrated Communication and Sensing, Ministry of Education, Guangdong University of Technology, Guangzhou 510006, China

<sup>c</sup>Guangdong Provincial Key Laboratory of Photonics Information Technology, Advanced Institute of Photonics Technology, School of Information Engineering, Guangdong University of Technology, Guangzhou 510006, China. E-mail: gaozhensen@gdut.edu.cn

<sup>d</sup>Innovation Center for Gallium Oxide Semiconductor (IC-GAO), College of Integrated Circuit Science and Engineering, Nanjing University of Posts and Telecommunications, Nanjing 210023, China. E-mail: whtang@njupt.edu.cn


method to stabilize the crystal structure against thermal processes, making it a possible approach to obtain  $\text{Ga}_2\text{O}_3$  with a thermally stabilized metastable phase and preventing the transition to the  $\beta$ -phase.<sup>23–25</sup> Acting as a satisfying high-quality  $\text{Ga}_2\text{O}_3$  on hetero-substrates for developing high-performance wide-band-gap optoelectronic devices, metastable  $\gamma$ -phase  $\text{Ga}_2\text{O}_3$  is considered here. Hiroyuki *et al.* have demonstrated the fabrication of Mn-doped  $\gamma$ - $\text{Ga}_2\text{O}_3$  at a temperature of 500 °C on  $\alpha$ - $\text{Al}_2\text{O}_3$  (0001) substrates using the PLD method, which differs from the undoped film that shows the  $\beta$  phase.<sup>26</sup> Sam-Dong *et al.* have shown the enhancement of thermal stability of  $\alpha$ - $\text{Ga}_2\text{O}_3$  films on sapphire substrates upon Al doping. The films can be grown at a temperature as high as 800 °C and can withstand an annealing temperature as high as 850 °C without forming the  $\beta$  phase.<sup>23</sup> Furthermore, Yue *et al.* have reported the synthesis of metastable  $\gamma$ - $\text{Ga}_2\text{O}_3$  nanoflowers with hexagonal nanopetals by the oxidation of metallic Ga in solutions.<sup>27</sup> The  $\gamma$ - $\text{Ga}_2\text{O}_3$  nanoflowers show excellent solar-blind detection performance; however, the poor thermal stability of the metastable phase still hinders the target application. Until now, the difficulty in synthesizing single-phase crystals and the poor thermal stability of the metastable  $\gamma$ -phase of  $\text{Ga}_2\text{O}_3$  have greatly limited its potential applications in wide-band-gap high-performance optoelectronic devices.

In this work, the Al-doped  $\gamma$ - $\text{Ga}_2\text{O}_3$  thin film was epitaxially grown on  $\alpha$ - $\text{Al}_2\text{O}_3$  (0001) substrates using the radio frequency magnetron sputtering technique, with the growth temperature successfully increased to 750 °C. A solar blind PD based on Al-doped  $\gamma$ - $\text{Ga}_2\text{O}_3$  thin film was successfully constructed. The PD shows excellent photoelectric properties. The  $\gamma$ - $\text{Ga}_2\text{O}_3$  thin film-based PDs might open up new possibilities for obtaining high-performance thin film-based solar blind UV optoelectronic devices.

## 2. Experimental section

### 2.1. Preparation and characterization of $\text{Ga}_2\text{O}_3$ thin films

The film samples were prepared on top of (0001) oriented single-crystal  $\alpha$ - $\text{Al}_2\text{O}_3$  substrates using radio frequency (RF) magnetron sputtering. The  $\text{Ga}_2\text{O}_3$  ceramic ( $\pi \times 30^2 \times 8 \text{ mm}^3$ , 99.99% purity) with/without embedded  $\text{Al}_2\text{O}_3$  ceramic ( $\pi \times 12.5^2 \times 4 \text{ mm}^3$ , 99.99% purity) was used as a target for Al-doped/pure  $\text{Ga}_2\text{O}_3$  thin film preparations, respectively. In the experiment, the  $\text{Al}_2\text{O}_3$  target was covered at the glow circle position of the  $\text{Ga}_2\text{O}_3$  target, and the incorporation amount was fine-tuned by varying the size of the coverage area. The base pressure in the chamber was  $1 \times 10^{-4} \text{ Pa}$ , and the distance between the  $\text{Ga}_2\text{O}_3$  target and the substrate was 6 cm. The flow rate of Ar (99.999% purity) gas was fixed to 24 sccm by a mass flow controller. The films were deposited at a working pressure of 1 Pa and RF power of 70 W for 2 h. The substrate temperature was fixed at 750 °C. The crystal structures of the as-grown films were investigated by a PANalytical X'pert PRO diffractometer using  $\text{Cu K}\alpha$  ( $\lambda = 1.5405 \text{ \AA}$ ) radiation. The structural quality was estimated by X-ray rocking curve (XRC) measurements using Smart Lab X-ray diffraction (XRD). The surface morphologies were characterized by a Hitachi S-4800 field emission scanning

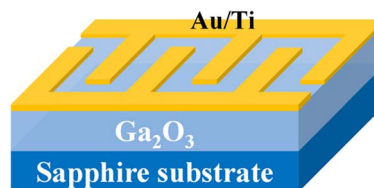


Fig. 1 Schematic of an MSM structure PD.

electron microscope (FE-SEM). UV-visible (UV-vis) absorption spectra were taken using a Hitachi U-3900 UV-vis spectrophotometer. The elemental content was analyzed using X-ray photoelectron spectroscopy (XPS).

### 2.2. Fabrication and characterization of the photodetector

To construct a metal–semiconductor–metal (MSM) PD, a three-pair interdigital Au/Ti electrode was deposited on the film by RF magnetron sputtering, as illustrated in Fig. 1. The Au/Ti electrode is chosen because the affinity of  $\text{Ga}_2\text{O}_3$  is close to the work function of Ti, making it easy to form ohmic contact. The width and length of the electrode fingers were 200  $\mu\text{m}$  and 2800  $\mu\text{m}$ , respectively. The spacing gap was 200  $\mu\text{m}$ . A small point electrode ( $\sim 0.1 \text{ mm}$  diameter) of indium metal was also pressed onto the Au/Ti electrode as connection points with a Cu wire. A Keithley 2450 source meter was utilized to measure the current–voltage ( $I$ – $V$ ) and time-dependent photoresponse of the  $\text{Ga}_2\text{O}_3$  film-based PD. A UV lamp ( $\sim 7 \text{ W}$ ) with wavelengths of 254 nm and 365 nm was used as the light source, and the light irradiation power density was tuned by adjusting the distance between the light source and the sample.

## 3. Results and discussion

The XRD patterns of undoped and Al-doped  $\text{Ga}_2\text{O}_3$  thin films are shown in Fig. 2(a). The undoped  $\text{Ga}_2\text{O}_3$  thin film formed on the  $\alpha$ - $\text{Al}_2\text{O}_3$  substrate is a monoclinic  $\beta$  phase, as determined by XRD (JCPDS Card No. 43-1012). Besides the diffraction peaks of the  $\text{Al}_2\text{O}_3$  substrate, diffraction peaks located at around 18.88°, 38.17°, and 58.88° are observed for the undoped film, which corresponds well to the  $\beta$  (201),  $\beta$  (402) and  $\beta$  (603) lattice planes, respectively. The Al-doped  $\text{Ga}_2\text{O}_3$  thin film formed on the  $\alpha$ - $\text{Al}_2\text{O}_3$  substrate is a cubic  $\gamma$  phase, as determined by XRD (JCPDS Card No. 20-0426). Besides the diffraction peaks of the  $\text{Al}_2\text{O}_3$  substrate, diffraction peaks located at around 18.67°, 37.85°, and 58.49° are observed for the Al-doped film, which corresponds well to the  $\gamma$  (111),  $\gamma$  (222) and  $\gamma$  (333) lattice planes, respectively. The X-ray rocking curves of  $\gamma$ - $\text{Ga}_2\text{O}_3$  (111) and  $\beta$ - $\text{Ga}_2\text{O}_3$  (201) planes are shown in Fig. 2(b) and (c) for the Al-doped and undoped films, respectively, and correspond to the FWHM values of 3672 and 5184 arcsec. The result indicates that the crystal quality of the as-grown  $\gamma$ - $\text{Ga}_2\text{O}_3$  film is better than that of the  $\beta$ - $\text{Ga}_2\text{O}_3$  film, the preparation conditions of which are similar.

The top-view SEM morphologies of the Al-doped  $\gamma$ - $\text{Ga}_2\text{O}_3$  film and undoped  $\beta$ - $\text{Ga}_2\text{O}_3$  film are presented in Fig. 3(a). It is obvious that the  $\gamma$ - $\text{Ga}_2\text{O}_3$  and  $\beta$ - $\text{Ga}_2\text{O}_3$  films appear to form



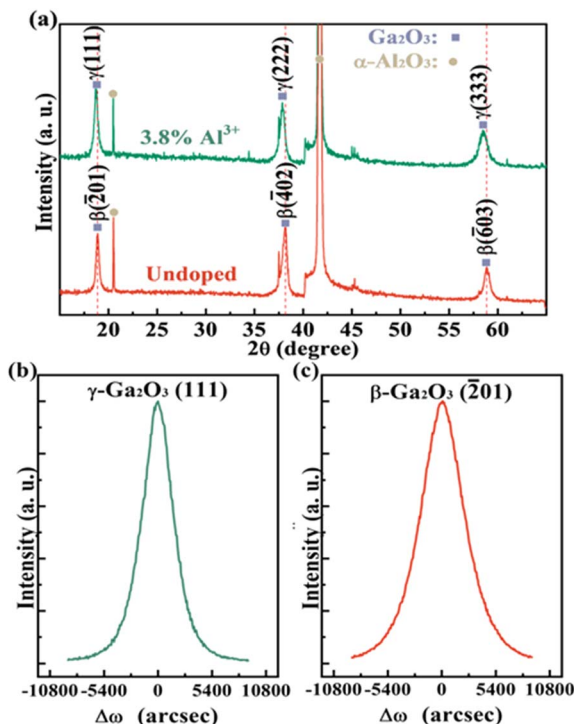


Fig. 2 (a) XRD patterns of undoped and Al-doped  $\text{Ga}_2\text{O}_3$  films. X-ray rocking curves of (b)  $\gamma\text{-Ga}_2\text{O}_3$  (111) for the Al-doped film and (c)  $\beta\text{-Ga}_2\text{O}_3$  (201) for the undoped film.

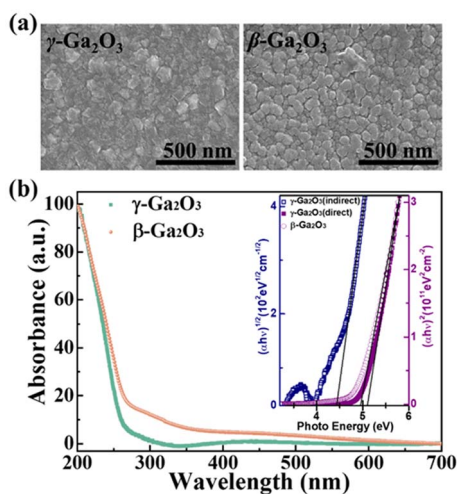


Fig. 3 (a) SEM images of the Al-doped  $\gamma\text{-Ga}_2\text{O}_3$  and undoped  $\beta\text{-Ga}_2\text{O}_3$  films. (b) UV-vis absorbance spectra of the Al-doped  $\gamma\text{-Ga}_2\text{O}_3$  and undoped  $\beta\text{-Ga}_2\text{O}_3$  films with the plot of  $(\alpha h\nu)^2$  and  $(\alpha h\nu)^{1/2}$  vs.  $h\nu$  in the inset.

different surface structures on (0001) sapphire substrates. For the  $\gamma\text{-Ga}_2\text{O}_3$  film, irregular pseudo-pyramid structures are distributed randomly on the surface, and the grain boundary is not clear; a similar surface structure has been observed for cubic- $\text{In}_2\text{O}_3$  on (0001) sapphire substrates in our previous study.<sup>28</sup> The surface structures of the  $\beta\text{-Ga}_2\text{O}_3$  film are columnar-like, and a clear grain boundary can be observed.

Fig. 3(b) shows the UV-vis absorbance spectrum of the Al-doped  $\gamma\text{-Ga}_2\text{O}_3$  film and the undoped  $\beta\text{-Ga}_2\text{O}_3$  film. It is evident that all the films have significant absorption edges at  $\sim 250$  nm, near the lower edge of the solar-blind region. Moreover, the bandgap of the semiconductor film can be evaluated by extrapolating the linear region of the plots of  $(\alpha h\nu)^2$  and  $(\alpha h\nu)^{1/2}$  versus  $h\nu$  for direct and indirect transitions, respectively. For  $\beta$ -phase  $\text{Ga}_2\text{O}_3$ , a direct bandgap semiconductor, the bandgap value was determined to be 4.94 eV, as shown in the inset of Fig. 3(b). As the transition type of  $\gamma$ -phase  $\text{Ga}_2\text{O}_3$  is undefined, both the direct and indirect bandgaps were estimated for the Al-doped  $\gamma\text{-Ga}_2\text{O}_3$  film. The direct and indirect bandgap values were determined to be 5.08 and 4.43 eV, respectively, which were slightly higher than those for undoped  $\gamma\text{-Ga}_2\text{O}_3$  (5.0 and 4.4 eV, respectively).<sup>19</sup>

XPS analysis was performed to elucidate the chemical compositions and oxygen deficiency in the as-grown films. The surface of the films was etched by  $\text{Ar}^+$  bombardment before the XPS measurement. Fig. 4(a) shows the wide survey spectrum in the binding energy range from  $-40$  eV to  $1350$  eV to identify the elements in the Al-doped  $\gamma\text{-Ga}_2\text{O}_3$  film. XPS peaks of Ga, O, Al and C were indicated in the Figure, and there were no other elements detected from the wide survey spectrum of the film. The charge-shift spectrum was calibrated using the C 1s peak at 284.8 eV. The Al 2p core level peak of the Al-doped  $\gamma\text{-Ga}_2\text{O}_3$  film is presented in Fig. 4(b), and the energy peak center is observed at 71.1 eV. The peak position shows a significant shift compared to the Al 2p peak in pure  $\text{Al}_2\text{O}_3$  film on the same substrate (74.5 eV). A similar phenomenon was also observed with a negative shift for the Al 2p peak during the formation of Al–O–Ga bonds.<sup>14</sup> In their report, the peak position was noted at 73.9 eV in the  $(\text{Al}_{0.22}\text{Ga}_{0.78})_2\text{O}_3$  film; the significant shift in our result indicates that Al is present in the Al-doped  $\gamma\text{-Ga}_2\text{O}_3$  film in the form of Al–O–Ga bonds. We have not yet identified whether the Al–O–Ga bonds are the key factors to obtain stabilized  $\gamma\text{-Ga}_2\text{O}_3$ , but they are a very significant sign to understand if the growing film is in the  $\gamma$  phase or not. The Ga 3d core level peaks of the Al-doped  $\gamma\text{-Ga}_2\text{O}_3$  and undoped  $\beta\text{-Ga}_2\text{O}_3$  films are shown in Fig. 4(c), with the energy peak centers observed at 19.7 eV and 20.1 eV, respectively. The O 1s core level peaks of the Al-doped  $\gamma\text{-Ga}_2\text{O}_3$  and undoped  $\beta\text{-Ga}_2\text{O}_3$  films are shown in Fig. 4(d), and the energy peaks are observed at 530.2 eV and 530.6 eV, respectively. The O 1s peaks can be divided into two components: I and II; peak I is attributed to lattice oxygen ions, and peak II is attributed to the oxygen ions in the oxygen vacancy region and surface defects of the film.<sup>5,10</sup> The intensity of oxygen vacancies and surface defects in the film has a significant negative influence on the performance of  $\text{Ga}_2\text{O}_3$  thin film-based PDs, such as dark current and response speed.<sup>29</sup> The peak ratios of II/I were 1/5 and 1/3 for Al-doped  $\gamma\text{-Ga}_2\text{O}_3$  and pure  $\beta\text{-Ga}_2\text{O}_3$ , respectively [Fig. 4(d)], which indicates a lower intensity of oxygen vacancies and surface defects in the Al-doped  $\gamma\text{-Ga}_2\text{O}_3$  film than in the pure  $\beta\text{-Ga}_2\text{O}_3$  film.

Fig. 5 shows the room-temperature  $I$ - $V$  characteristics of the PD based on an Al-doped  $\gamma\text{-Ga}_2\text{O}_3$  thin film in the dark, under 365 nm ( $100 \mu\text{W cm}^{-2}$ ) and 254 nm (with various light intensities) light illumination. The  $I$ - $V$  curve in the dark is linear,





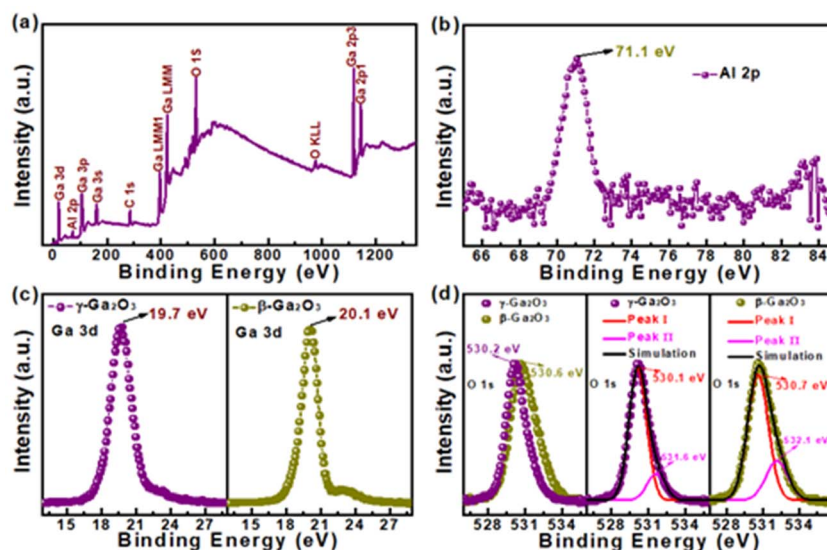


Fig. 4 (a) XPS wide survey spectrum and (b) core level of Al 2p for the Al-doped  $\gamma$ -Ga<sub>2</sub>O<sub>3</sub> film. Core levels of (c) Ga 3d and (d) O 1s for Al-doped  $\gamma$ -Ga<sub>2</sub>O<sub>3</sub> and undoped  $\beta$ -Ga<sub>2</sub>O<sub>3</sub> films.

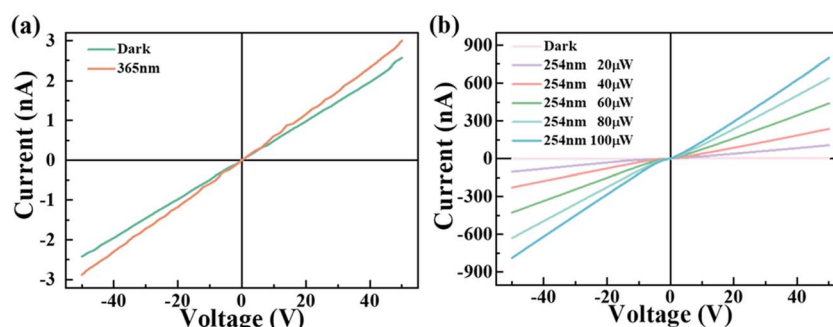


Fig. 5 (a)  $I$ - $V$  characteristics of the Al-doped  $\gamma$ -Ga<sub>2</sub>O<sub>3</sub> thin film-based MSM structure PD in the dark and under a 365 nm light illumination. (b)  $I$ - $V$  characteristics of the device in the dark and under a 254 nm light illumination with various light intensities.

indicating that the contact is of an ohmic type. The corresponding resistance is 19.5 G $\Omega$ , and the dark current is about 2.57 nA at a voltage of 50 V, as shown in Fig. 5(a), which is much lower than that of undoped  $\beta$ -Ga<sub>2</sub>O<sub>3</sub> films (about 100 nA at a voltage of 10 V), as per our previous reports. The  $I$ - $V$  curve under 365 nm light illumination indicates that the device is almost insensitive to 365 nm light illumination, as shown in Fig. 5(a). Meanwhile, the device has significant sensitivity for 254 nm light illumination, as shown in Fig. 5(b).

In order to further investigate the performance of the Al-doped  $\gamma$ -Ga<sub>2</sub>O<sub>3</sub> thin film-based PD, the time-dependent photoresponse to solar-blind UV illuminations was investigated, as shown in Fig. 6. Fig. 6(a) and (b) show the time-dependent photoresponse of the device to 254 nm UV light illuminations with varied light intensities and bias voltages, respectively. The device shows excellent photoelectric performance, with the photocurrent gradually increasing with increasing incident light intensities and bias voltages. The larger the voltage applied, the higher the  $I_{\text{photo}}$  obtained, following the basic photoconductance rule, which works as a photo-sensitive

resistance. The higher the light intensity, the higher the  $I_{\text{photo}}$  output, as more photo-generated carriers would be devoted to  $I_{\text{photo}}$  at a certain voltage. Another important performance parameter of solar blind PDs is the response time. To study the response time of the device, the current rising and decaying process can be derived by fitting the photoresponse curve with the following relaxation equation:<sup>30</sup>

$$I = I_0 + Ae^{-t/\tau_1} + Be^{-t/\tau_2} \quad (1)$$

where  $I_0$  is the photocurrent in the steady state,  $A$  and  $B$  are the constant values,  $t$  is the time, and  $\tau_1$  and  $\tau_2$  are the relaxation time constants. As shown in Fig. 6(c) and (d), the photoresponse processes fit quite well. We note that the rising edge consists of two components ( $\tau_{r1}$  and  $\tau_{r2}$ ), and the decaying edge is steep, consisting of only one component. It has been estimated that the rise edge constants  $\tau_{r1}$  and  $\tau_{r2}$  are around 2.39 s/12.57 s, 1.52 s/8.16 s, 1.02 s/6.92 s and 0.88 s/5.89 s for the device under 20  $\mu\text{W cm}^{-2}$ , 40  $\mu\text{W cm}^{-2}$ , 60  $\mu\text{W cm}^{-2}$  and 80  $\mu\text{W cm}^{-2}$  light illuminations at a bias voltage of 50 V, respectively. In contrast, the rise edge constants  $\tau_{r1}$  and  $\tau_{r2}$  are estimated to be 1.22 s/



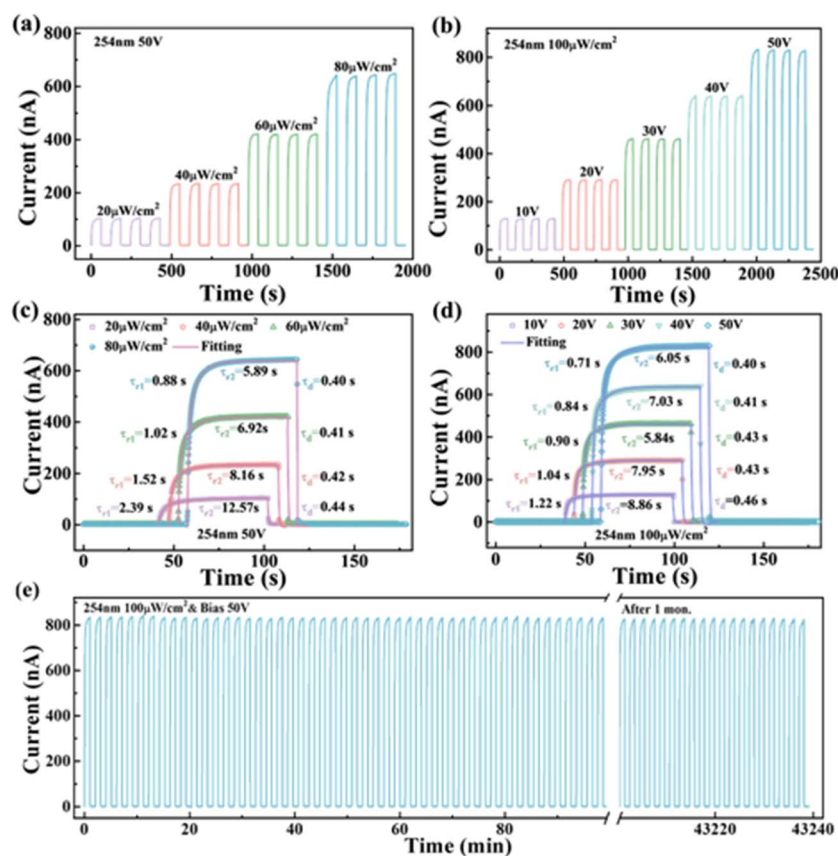


Fig. 6 Time-dependent photoresponse of the Al-doped  $\gamma$ -Ga<sub>2</sub>O<sub>3</sub> thin film-based MSM structure PD measured under different conditions: (a) photoresponse of the device under different light intensities at 50 V; (b) photoresponse of the device at different bias voltages under 100  $\mu\text{W cm}^{-2}$ ; (c) experimental curve and fitted curve of the current rising and decaying process of the device under different light intensities at 50 V; (d) experimental curve and fitted curve of the current rising and decaying process of the device at different bias voltages under 100  $\mu\text{W cm}^{-2}$ ; (e) photoresponse stability of the device during a long time test and after storage for one month.

8.86 s, 1.04 s/7.95 s, 0.90 s/5.84 s, 0.84 s/7.03 s and 0.71 s/6.05 s for the device under 100  $\mu\text{W cm}^{-2}$  light illuminations at bias voltages of 10 V, 20 V, 30 V, 40 V and 50 V, respectively. It is obvious that the rise speed increases with both light intensity and bias voltage. Generally, the fast-response component can be attributed to the rapid change in carrier concentration that occurs as soon as the light is turned on or off, while the slow-response component is caused by carrier trapping/releasing owing to the existence of oxygen vacancies and other surface defects in the Al-doped  $\gamma$ -Ga<sub>2</sub>O<sub>3</sub> film. It is evident that, when there are plenty of photon-generated carriers under stronger intensities of light illumination, the trapping/releasing effect is easier to saturate, so the response time is shorter; when the applied bias voltage is higher, the photo-generated electrons and holes undergo a rapid separation and then transfer toward the corresponding electrodes, resulting in a faster response speed. The decay edge constants  $\tau_d$  are estimated to be 0.44 s, 0.42 s, 0.41 s and 0.40 s for the device under 20  $\mu\text{W cm}^{-2}$ , 40  $\mu\text{W cm}^{-2}$ , 60  $\mu\text{W cm}^{-2}$  and 80  $\mu\text{W cm}^{-2}$  light illuminations at a bias voltage of 50 V, respectively. The decay edge constants  $\tau_d$  are estimated to be 0.46 s, 0.43 s, 0.43 s, 0.41 s and 0.40 s for the device under 100  $\mu\text{W cm}^{-2}$  light illumination at bias voltages of

10 V, 20 V, 30 V, 40 V and 50 V, respectively. Due to the absence of oxygen vacancies in Al doped  $\gamma$ -Ga<sub>2</sub>O<sub>3</sub> film, the trapping/releasing effect is a localization transport process without plentiful of photon-generated carriers when the light is off. It can hardly influence the photoconductance of the device, so the decaying edge is quite steep.

To quantitatively assess the device performance of the present solar blind photodetector, both responsivity ( $R_\lambda$ ) and detectivity ( $D^*$ ) were calculated, as shown in Fig. 7(a) and (c) as a function of light intensity and bias voltage, respectively.  $R_\lambda$ , which is defined as the photocurrent generated per unit power of incident light on the effective area of a PD, is calculated by the following equation:<sup>2</sup>

$$R_\lambda = (I_{\text{light}} - I_{\text{dark}})/(P_\lambda \cdot S) \quad (2)$$

where  $I_{\text{light}}$  is the light current,  $I_{\text{dark}}$  is the dark current of the device when illuminated with a light source,  $P_\lambda$  is the light intensity illuminated on the device,  $S$  is the effective illuminated area ( $S = 3.24 \text{ mm}^2$ ), and  $\lambda$  is the wavelength of the illuminating light.

Detectivity, which is usually used to evaluate the smallest detectable of a PD, can be calculated as follows:<sup>31</sup>



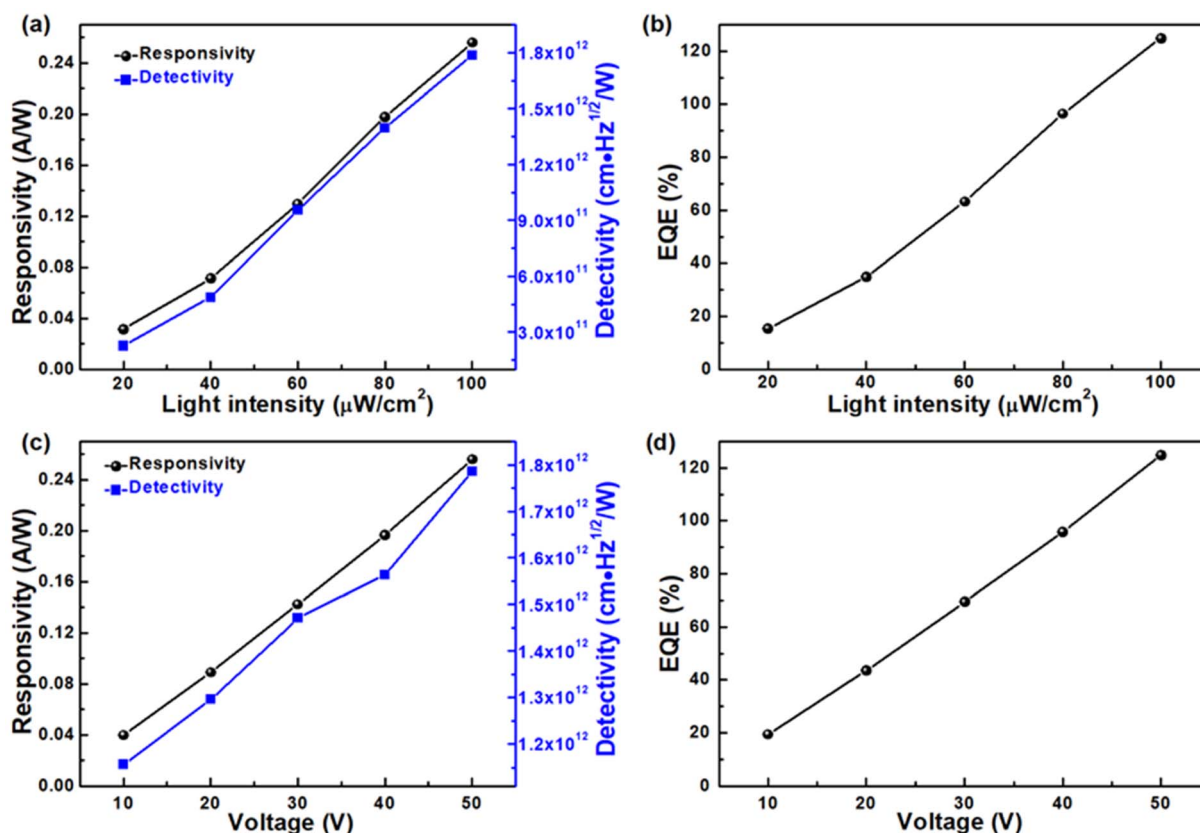


Fig. 7 (a) Responsivity and detectivity of the Al-doped  $\gamma$ -Ga<sub>2</sub>O<sub>3</sub> thin film-based MSM structure PD as a function of bias voltage. (b) External quantum efficiency of the device as a function of bias voltage. (c) Responsivity and detectivity of the device as a function of light intensity. (d) External quantum efficiency of the device as a function of light intensity.

$$D^* = \frac{R_\lambda A^{1/2}}{(2eI_{\text{dark}})^{1/2}} \quad (3)$$

where  $R_\lambda$  is the responsivity,  $A$  is the effective area of the present device channel ( $A = 3.24 \text{ mm}^2$ ),  $e$  is the electronic charge, and  $I_{\text{dark}}$  is the dark current. It is clear that both the  $R_\lambda$  and  $D^*$  values increase with increasing light intensity and bias voltage. Specifically, the responsivity and detectivity are as high as  $0.26 \text{ A W}^{-1}$  and  $1.79 \times 10^{12}$  under  $100 \text{ μW cm}^{-2}$  light illumination at  $50 \text{ V}$ , respectively. Notably, the present device exhibits no obvious performance degradation with increasing light intensity and bias voltage, indicating that the device has good self-heating dissipation. Moreover, the external quantum efficiency (EQE) is also the key parameter to evaluate the performance of a PD, which is defined as the number of electrons probed per incident photon and can be calculated as follows:<sup>32</sup>

$$\text{EQE} = \frac{hcR_\lambda}{e\lambda} \quad (4)$$

where  $R_\lambda$  is the responsivity,  $h$  is Planck's constant,  $c$  is the velocity of light,  $e$  is the electronic charge, and  $\lambda$  is the exciting wavelength of the solar blind light. The EQE gradually increases with increasing light intensity and bias voltage, reaching a maximum of  $124.92\%$  under  $100 \text{ μW cm}^{-2}$  light illumination at  $50 \text{ V}$ , as shown in Fig. 7(b) and (d).

In order to investigate the spectral selectivity of the present device, the spectral responsivity was measured in the range of  $225$  to  $600 \text{ nm}$ , as shown in Fig. 8. It can be observed that the device shows excellent wavelength selectivity: it has highest responsivity at a wavelength of about  $230 \text{ nm}$ ; as the wavelength increases, the responsivity gradually decreases and reaches

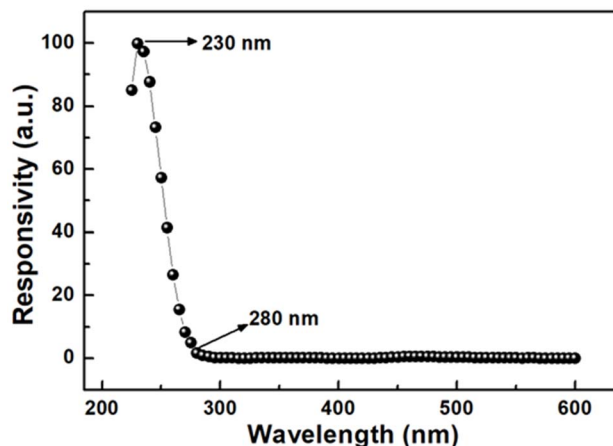


Fig. 8 Normalized spectral selectivity of the Al-doped  $\gamma$ -Ga<sub>2</sub>O<sub>3</sub> thin film-based MSM structure PD.



a minimum value at about 280 nm. The rejection ratio of responsivity values for the solar blind region *versus* the solar visible region was estimated by dividing the responsivity at 230 nm by that at 280 nm. The excellent rejection ratio was evaluated at 60.98, indicating an excellent solar-blind UV response. The higher rejection ratio can be attributed to the better crystal quality and the absence of oxygen vacancies in Al-doped  $\gamma$ -Ga<sub>2</sub>O<sub>3</sub>.<sup>33</sup>

## 4. Conclusion

The Al-doped  $\gamma$ -Ga<sub>2</sub>O<sub>3</sub> thin film was epitaxially grown on  $\alpha$ -Al<sub>2</sub>O<sub>3</sub> (0001) substrates by radio frequency magnetron sputtering, and the growth temperature was successfully increased to 750 °C. The solar blind UV PD based on the as-grown thin film exhibits excellent solar-blind UV photoelectric properties. Under 100  $\mu$ W cm<sup>-2</sup> 254 nm light illumination at a bias voltage of 50 V, the device exhibits a rise and decay time of 0.71 s/6.05 s and 0.40 s, responsivity of 0.26 A W<sup>-1</sup>, detectivity of  $1.79 \times 10^{12}$ , and an EQE of 124.92%, along with high stability and reproducibility. Remarkably, the present device exhibits no obvious performance degradation with increasing light intensity and bias voltage. It indicates that the device has good self-heating dissipation, which will be beneficial for future practical applications. Moreover, the device shows excellent wavelength selectivity with a solar blind/visible rejection ratio of 60.98, which is nearly blind to photons with wavelengths longer than 280 nm. These results suggest that  $\gamma$ -Ga<sub>2</sub>O<sub>3</sub> thin film-based PDs can open up new possibilities for obtaining high performance thin film-based solar blind UV optoelectronic devices.

## Conflicts of interest

There are no conflicts of interest to declare.

## Data availability

The data supporting this article are available from the corresponding author upon reasonable request.

## Acknowledgements

National Key R&D Program of China (2023YFB2906000); National Natural Science Foundation of China (62375055); Guangdong Basic and Applied Basic Research Foundation (2023B1515020088); Basic and Applied Basic Research Project of Guangzhou Basic Research Program (2025A04J5417) and the Start-Up Funding of Guangdong Polytechnic Normal University (2022SDKYA013) are greatly acknowledged.

## References

- 1 Y. Zhao, J. Zhang, D. Jiang, *et al.*, Ultraviolet photodetector based on a MgZnO film grown by radio-frequency magnetron sputtering, *ACS Appl. Mater. Interfaces*, 2009, **1**(11), 2428–2430.
- 2 W. Cui, D. Y. Guo, X. L. Zhao, *et al.*, Solar-blind photodetector based on Ga<sub>2</sub>O<sub>3</sub> nanowires array film growth from inserted Al<sub>2</sub>O<sub>3</sub> ultrathin interlayers for improving responsivity, *RSC Adv.*, 2016, **6**(103), 100683–100689.
- 3 Z. Li, T. Yan and X. Fang, Low-dimensional wide-bandgap semiconductors for UV photodetectors, *Nat. Rev. Mater.*, 2023, **8**(9), 587–603.
- 4 X. Zhu, Y. Wu, Z. Pan, *et al.*, Advancements in Ga<sub>2</sub>O<sub>3</sub>-based heterojunction ultraviolet photodetectors: Types, fabrication techniques, and integrated materials for enhancing photoelectric conversion efficiency, *J. Alloys Compd.*, 2025, **1010**, 177757.
- 5 Y. H. An, Z. S. Gao, Y. Guo, *et al.*, One  $\epsilon$ -Ga<sub>2</sub>O<sub>3</sub>-based solar-blind Schottky photodetector emphasizing high photocurrent gain and photocurrent-intensity linearity, *Chin. Phys. B*, 2023, **32**(5), 058502.
- 6 Y. Li, T. Tokizono, M. Liao, *et al.*, Efficient Assembly of Bridged  $\beta$ -Ga<sub>2</sub>O<sub>3</sub> Nanowires for Solar-Blind Photodetection, *ACS Appl. Mater. Interfaces*, 2010, **20**(22), 3972–3978.
- 7 Y. Gao, J. Yang, X. Ji, *et al.*, Semipolar (1122) AlGaN-based solar-blind ultraviolet photodetectors with fast response, *ACS Appl. Mater. Interfaces*, 2022, **14**(18), 21232–21241.
- 8 M. M. Fan, K. W. Liu, X. Chen, *et al.*, Mechanism of Excellent Photoelectric Characteristics in Mixed-Phase ZnMgO Ultraviolet Photodetectors with Single Cutoff Wavelength, *ACS Appl. Mater. Interfaces*, 2015, **7**(37), 20600–20606.
- 9 J. Ye, S. Jin and Y. Cheng, Photocurrent ambipolar behavior in phase junction of a Ga<sub>2</sub>O<sub>3</sub> porous nanostructure for solar-blind light control logic devices, *ACS Appl. Mater. Interfaces*, 2024, **16**(20), 26512–26520.
- 10 R. Jin, J. Liu, S. Chen, *et al.*, Ultrasensitive Self-Powered Flexible Crystalline  $\beta$ -Ga<sub>2</sub>O<sub>3</sub>-Based Photodetector Obtained through Lattice Symmetry and Band Alignment Engineering, *ACS Appl. Mater. Interfaces*, 2024, **16**(32), 42406–42414.
- 11 T. Oshima, T. Okuno and S. Fujita, Ga<sub>2</sub>O<sub>3</sub> Thin Film Growth on Plane Sapphire Substrates by Molecular Beam Epitaxy for Deep-Ultraviolet Photodetectors, *Jpn. J. Appl. Phys.*, 2007, **46**(11R), 7217–7220.
- 12 Z. Y. Wang, G. Zhang, X. J. Zhang, *et al.*, Polarization-sensitive artificial optoelectronic synapse based on anisotropic  $\beta$ -Ga<sub>2</sub>O<sub>3</sub> single crystal for neuromorphic vision systems and information encryption, *Adv. Opt. Mater.*, 2024, **12**(29), 2401256.
- 13 T. Oshima, Y. Kato, M. Oda, *et al.*, Epitaxial growth of gamma-(Al<sub>x</sub>Ga<sub>1-x</sub>)O<sub>3</sub> alloy films for band-gap engineering, *Appl. Phys. Express*, 2017, **10**(5), 051104.
- 14 H. Xu, Y. Weng, K. Chen, *et al.*, Ultra-low BER encrypted communication based on self-powered bipolar photoresponse ultraviolet photodetector, *Adv. Opt. Mater.*, 2024, **10**, 2402238.
- 15 P. Li, L. Dong, C. Li, *et al.*, Indium doping-assisted monolayer Ga<sub>2</sub>O<sub>3</sub> exfoliation for performance-enhanced MOSFETs, *Nanoscale*, 2023, **15**(28), 12105–12115.
- 16 R. Roy, V. Hill and E. Osborn, Polymorphism of Ga<sub>2</sub>O<sub>3</sub> and the System Ga<sub>2</sub>O<sub>3</sub>-H<sub>2</sub>O, *J. Am. Chem. Soc.*, 1952, **74**(3), 719–722.





- 17 X. C. Xia, Y. P. Chen, Q. J. Feng, *et al.*, Hexagonal phase-pure wide band gap epsilon-Ga<sub>2</sub>O<sub>3</sub> films grown on 6H-SiC substrates by metal organic chemical vapor deposition, *Appl. Phys. Lett.*, 2016, **108**(20), 202103.
- 18 S. Fujita, M. Oda, K. Kaneko, *et al.*, Evolution of corundum-structured III-oxide semiconductors: Growth, properties, and devices, *Jpn. J. Appl. Phys.*, 2016, **55**(12), 1202A3.
- 19 T. Oshima, T. Nakazono, A. Mukai, *et al.*, Epitaxial growth of gamma-Ga<sub>2</sub>O<sub>3</sub> films by mist chemical vapor deposition, *J. Cryst. Growth*, 2012, **359**(15), 60–63.
- 20 S. Yoshioka, H. Hayashi, A. Kuwabara, *et al.*, Structures and energetics of Ga<sub>2</sub>O<sub>3</sub> polymorphs, *J. Phys.: Condens. Matter*, 2007, **19**(34), 346211.
- 21 H. Nishinaka, D. Tahara and M. Yoshimoto, Heteroepitaxial growth of epsilon-Ga<sub>2</sub>O<sub>3</sub> thin films on cubic (111) MgO and (111) yttria-stabilized zirconia substrates by mist chemical vapor deposition, *Jpn. J. Appl. Phys.*, 2016, **55**(12), 1202BC.
- 22 S. X. Ge and Z. Zheng, Phase controllable synthesis of unusual epsilon-Ga<sub>2</sub>O<sub>3</sub> single crystals with promising luminescence property, *Solid State Sci.*, 2009, **11**(9), 1592–1596.
- 23 S. D. Lee, Y. Ito, K. Kaneko, *et al.*, Enhanced thermal stability of alpha gallium oxide films supported by aluminum doping, *Jpn. J. Appl. Phys.*, 2015, **54**(3), 030301.
- 24 R. Lorenzi, N. V. Golubev, E. S. Ignat'eva, *et al.*, Defect-assisted photocatalytic activity of glass-embedded gallium oxide nanocrystals, *J. Colloid Interface Sci.*, 2022, **608**(3), 2830–2838.
- 25 G. Yang, H. A. Ni, H. D. Liu, *et al.*, The doping effect on the crystal structure and electrochemical properties of LiMn<sub>x</sub>M<sub>1-x</sub>PO<sub>4</sub> (M = Mg, V, Fe, Co, Gd), *J. Power Sources*, 2011, **196**(10), 4747–4755.
- 26 H. Hayashi, R. Huang, H. Ikeno, *et al.*, Room temperature ferromagnetism in Mn-doped gamma-Ga<sub>2</sub>O<sub>3</sub> with spinel structure, *Appl. Phys. Lett.*, 2006, **89**(18), 181903.
- 27 Y. Teng, L. X. Song, A. Ponchel, *et al.*, Self-Assembled Metastable gamma-Ga<sub>2</sub>O<sub>3</sub> Nanoflowers with Hexagonal Nanopetals for Solar-Blind Photodetection, *Adv. Mater.*, 2014, **26**(36), 6238–6243.
- 28 W. Cui, X. L. Zhao, Y. H. An, *et al.*, Direct charge carrier injection into Ga<sub>2</sub>O<sub>3</sub> thin films using an In<sub>2</sub>O<sub>3</sub> cathode buffer layer: their optical, electrical and surface state properties, *J. Phys. D Appl. Phys.*, 2017, **50**(13), 135109.
- 29 D. Guo, P. Li, Z. Wu, *et al.*, Inhibition of unintentional extra carriers by Mn valence change for high insulating devices, *Sci. Rep.*, 2016, **6**(1), 24190.
- 30 D. Y. Guo, Z. P. Wu, P. G. Li, *et al.*, Fabrication of beta-Ga<sub>2</sub>O<sub>3</sub> thin films and solar-blind photodetectors by laser MBE technology, *Opt. Mater. Express*, 2014, **4**(5), 1067–1076.
- 31 W. Y. Kong, G. A. Wu, K. Y. Wang, *et al.*, Graphene-beta-Ga<sub>2</sub>O<sub>3</sub> Heterojunction for Highly Sensitive Deep UV Photodetector Application, *Adv. Mater.*, 2016, **28**(48), 10725.
- 32 J. M. Wu and W. E. Chang, Ultrahigh Responsivity and External Quantum Efficiency of an Ultraviolet-Light Photodetector Based on a Single VO<sub>2</sub> Microwire, *ACS Appl. Mater. Interfaces*, 2014, **6**(16), 14286–14292.
- 33 A. S. Pratiyush, S. Krishnamoorthy, S. V. Solanke, *et al.*, High responsivity in molecular beam epitaxy grown beta-Ga<sub>2</sub>O<sub>3</sub> metal semiconductor metal solar blind deep-UV photodetector, *Appl. Phys. Lett.*, 2017, **110**(22), 221107.

